Least-squares migration imaging of receiver functions

Yunfeng Chen[1], Yu Jeffrey Gu[2], Quan Zhang[1], Hang Wang[1], Pengfei Zhuo[3]and Yangkang Chen[4]

[1]Key Laboratory of Geoscience Big Data and Deep Resource of Zhejiang Province, School of Earth Sciences, Zhejiang University, Hangzhou, 310027, China
[2]Department of Physics, University of Alberta, Edmonton, AB, T6G 2E1, Canada
[3]College of Geoexploration Science and Technology, Jilin University, Changchun, 130026, China
[4]Bureau of Economic Geology, The University of Texas at Austin, University Station, Box X, Austin, Texas 78713-8924

Key Points:

- A least-squares migration method is developed for teleseismic receiver function imaging.
- Array processing techniques are adopted to develop a robust migration imaging workflow.
- Least-squares migration enables resolving fine-scale subsurface structures at significantly improved resolution than conventional methods.

Corresponding author: Yunfeng Chen, yunfeng_chen@zju.edu.cn

Abstract

The growth of data recorded by dense seismic arrays has stimulated the development of new array-based receiver function (RF) imaging techniques. This study examines the feasibility and performance of the least-squares migration (LSM) method, a state-of-art technique used in exploration seismology, to lithospheric imaging using teleseismic RFs. Taking advantage of a pair of forward (de-migration) and adjoint (migration) operators, the LSM casts migration as a regularized least-squares optimization problem. We employ the Split-step Fourier method to design the two operators and conduct wavefield propagation in heterogeneous media. Synthetic tests with models containing various Moho geometries demonstrate that LSM enables resolving interfaces at higher resolution than conventional migration. Then LSM is applied to teleseismic data recorded by the Hi-CLIMB array deployed on the Tibetan Plateau. Considering the irregular and noisy recordings from field acquisition, we adopt signal processing algorithms, including the Radon transform and Singular Spectrum Analysis filter, to regularize the wavefields and precondition the RFs. The proposed workflow produces a significantly improved subsurface image than conventional methods, revealing new observations of 1) two well-defined interfaces at the base of the crust and 2) gently dipping mantle discontinuities extending continuously from the Lhasa Block to the Qiangtang Block. These structures could represent the imbricated Indian and Tibetan crust underlain by the underthrusting Indian lithosphere, implying that the Indian collisional front extends as far north as the Bangong-Nujiang suture. Overall, our study offers a new high-resolution RF imaging tool and inspires the future development of advanced array processing workflows.

Plain Language Summary

The receiver function (RF) method is a widely applied approach that utilizes the converted waves to image the subsurface. We develop a new RF imaging method based on least-squares migration (LSM) from exploration seismology. This method allows projecting the energy recorded at surface receivers back to subsurface conversion points (i.e., migration). Unlike conventional methods, LSM optimizes the solution by fitting waveforms while simultaneously seeking a smooth model. We use synthetic data to test the proposed method and obtain much sharper Moho interfaces from LSM than those from the conventional approaches. We further assess the performance of LSM using earthquake data collected from the Hi-CLIMB array from the Tibetan Plateau. Because the noisy and irregular field data significantly degrade the reliability of seismic imaging, we utilize data processing methods to improve the quality of RFs before applying LSM. The resulting migration image reveals fine-scale structures that have not been imaged previously, which could have significant implications on the collision history between the Indian and Tibetan Plates. This work demonstrates the advantage of LSM in improving the resolution of subsurface images over conventional methods and calls for future efforts to develop advanced array imaging tools for better characterizing Earth's structure.

1 Introduction

Seismic imaging is a fundamental tool for probing the Earth's interior. Among various seismic imaging techniques, the receiver function (RF) method is widely used to constrain the structural layering, and elastic properties of the subsurface (Phinney, 1964; Vinnik, 1977; Langston, 1979). RF has been conventionally analyzed on a single station basis wherein a 1D seismic model is derived beneath the recording station using multiple earthquake recordings. In past decades, the rapid development of seismic sensing technology has revolutionized the acquisition, and earthquake data have been routinely recorded using dense seismic arrays. The extensive high-quality, densely-sampled array recordings enable the development of advanced seismic imaging methods for resolving fine-scale

subsurface structures. One popular array-based RF imaging method considers back-projecting the energy of converted waves to their conversion points (Dueker & Sheehan, 1998; Zhu, 2000) by tracing the ray paths through a 1D layered structure. On the other hand, migration imaging (Gray et al., 2001; Sava & Hill, 2009), a technique routinely applied in exploration seismology, has also been utilized to process teleseismic data. The migration method accounts for more complex laterally varying velocity structures and thus is becoming feasible and increasingly popular with dense seismic arrays that record the wavefield at a sub-kilometer scale. Over the years, several migration approaches have been proposed that, based on the assumption of wave propagation theory (i.e., modeling operator), can be generally classified into ray-theory and wave-equation-based methods. An early effort developed an inverse scattering approach based on 2D Born approximation and invert the scattered wave energy using the generalized Radon transform (Bostock et al., 2001). This method was well examined with numerical simulation (Shragge et al., 2001) and real data collected from the Cascadia subduction zone (Rondenay et al., 2001). Ryberg & Weber (2000) implemented a Kirchhoff approach and directly migrated the P-to-S converted energy on RFs. Cheng et al. (2016) extended the Kirchhoff migration to the 3D case by conducting ray-tracing with an eikonal equation while considering the P-to-S scattering pattern. This method has been successfully applied to image the slab in the subduction zone (Cheng et al., 2017) and discontinuities of the mantle transition zone (H. Zhang & Schmandt, 2019). Other migration approaches based on the ray-theory assumption have been implemented via employing Gaussian beam (Nowack et al., 2010) and plane-wave (Poppeliers & Pavlis, 2003a,b) propagation of seismic wavefields as well as through the construction of scattering kernels (Hansen & Schmandt, 2017). While these ray-theory methods offer a high-frequency asymptotic approximation of the single-scattering forward problem, a more rigorous assumption of wavefield propagation relies on solving the wave equation. L. Chen et al. (2005a) proposed a wave-equation post-stack migration method that solves one-way acoustic wave-equation with a phase screen propagator (Stoffa et al., 1990). The application of this method demonstrates improved imaging quality when applied to the Japan subduction zone (L. Chen et al., 2005b). Shragge et al. (2006) proposed a teleseismic short-profile migration approach that implemented the split-step Fourier approach to migrate the multimode scattered waves. More recently, Jiang et al. (2019) invoked the phase-shift plus interpolation method to forward and backward propagate the wavefields. Aside from these methods mentioned above, the time-domain finite-difference method has also been utilized to simulate the wave propagation in 2D (Shang et al., 2017), or 3D (Li et al., 2018; Millet et al., 2019) media.

These earlier studies mark important progress in applying teleseismic imaging techniques to improve subsurface structure. The least-squares migration (LSM), a method first proposed in the exploration seismology community (Nemeth et al., 1999; Kühl & Sacchi, 2003), is developed based on migration imaging and has been demonstrated to be a powerful technique to further improve the migration image. The migration process maps the diffraction energy back to the scattering points in the subsurface by designing a migration operator that is also the adjoint of the forward (de-migration) operator. Depending on the acquisition system and data quality, this operator is typically not an exact inverse of the forward process. Thus, the resulting migration image quality can be degraded by strong artifacts caused by an undersampled acquisition geometry and limited recording aperture. Comparatively, the LSM casts the migration process as an inverse problem by approximating the inverse of the forward-modeling operator and can reduce migration artifacts and improve the resolution of migration images. Despite its advantage over conventional migration techniques and successful application to exploration-scale imaging, the usage of LSM in migrating earthquake data remains thinly explored. Wilson & Aster (2005) proposed a regularized Kirchhoff migration approach to migrate multimode RF data. To the best of our knowledge, it is the first study that implemented the idea of least-squares migration, though it was more generally termed as the regularized migration. In this study, we continuously examine the feasibility, strength and limitation of LSM in teleseismic RF imaging. Our implementation of migration closely fol-

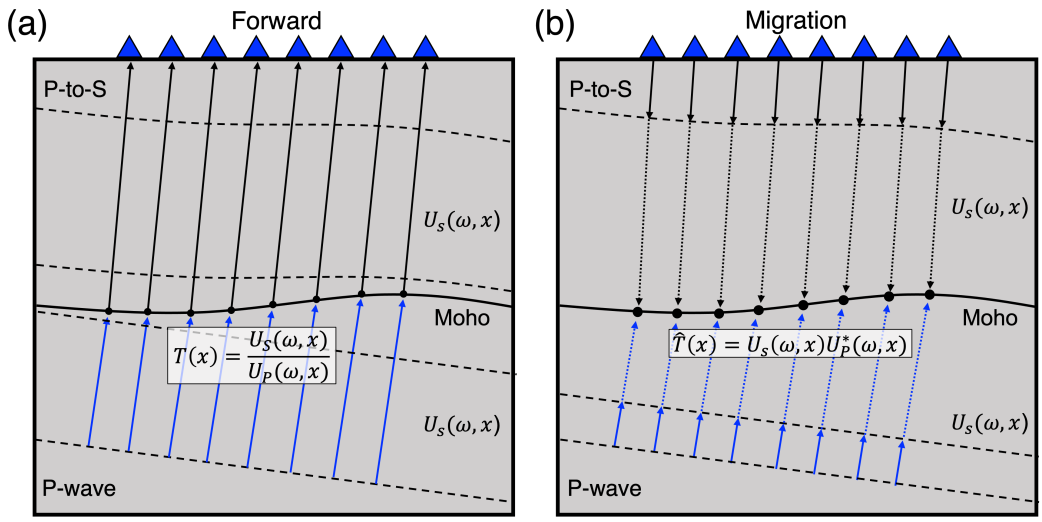

Figure 1. Schematic plots showing (a) forward propagation and (b) migration processes. The forward process conducts upward propagation of the planar P waves (blue ray paths), which propagate upon the Moho and convert into S waves (black ray paths), and then continuously propagate upward to receivers. The migration process forward (i.e., upward) propagates the P waves, and backward (i.e., downward) propagates the S waves, or more strictly speaking, converted waves on receiver functions. The position of conversion points (black circles) is located by applying certain imaging conditions, such as the cross-correlation condition used in our study. The dashed lines indicate the wavefront.

lows the teleseismic shot-profile migration approach proposed by Shragge et al. (2006). Mainly, the study first shows the formulation of LSM and explains the implementation details of the forward and adjoint operators. Then we run numerical experiments to test the proposed LSM method using two synthetic experiments. In a real data example, we develop an effective migration imaging workflow to resolve a few data-quality-related issues that restrict the practical application of LSM. We discuss key factors, including the data quality and spatial sampling on LSM results. Then we demonstrate the resolution improvement of the proposed LSM imaging workflow over the conventional RF imaging method (i.e., common conversion point stacking). Finally, we discuss a few limitations of the current implementation of LSM and suggest future improvements to the imaging workflow by accounting for a more rigorous treatment of wave propagation and more general acquisition geometry of seismic recordings. Overall, the proposed LSM method offers a new tool to take advantage of current seismic arrays and exploit methodologies highly tested in exploration seismology for improving subsurface imaging via teleseismic records.

2 Methods

2.1 Migration imaging

We describe the migration process in the context of the teleseismic incident wavefield. The forward propagation of the P-wave wavefield in a 2D media can be defined as

$$U_p(\omega, \mathbf{x}) = \mathbf{P}_u G(\omega, x, z), \tag{1}$$

where U_p is the up-going P-wave at a spatial location $\mathbf{x}$ in the frequency domain, $\mathbf{P}_u$ is the propagator, and $G(\omega, x, z)$ is the source function of the plane-wave for teleseismic

wavefield. Because the RF considers the P to S conversions, the recorded converted wavefield can be expressed as

$$U_s(\omega, x = r, z = 0) = \mathbf{\Psi S}_u U_s(\omega, \mathbf{x}), \tag{2}$$

where $U_s(\omega, x = r, z = 0)$ is the upward propagating S wavefield recorded at horizontal position r at the surface (i.e., $z = 0$), $\mathbf{\Psi}$ is the sampling operator that is 1 where data exists and 0 otherwise, and $\mathbf{S}_u$ is the corresponding propagator of S waves. The frequency-space representation of the up-going wavefield $U_s(\omega, \mathbf{x})$ is given by

$$U_s(\omega, \mathbf{x}) = U_p(\omega, \mathbf{x}) T(\mathbf{x}), \tag{3}$$

which states that the up-going S-wave is the multiplication of the incident P-wave and the effective transmission coefficient $T(\mathbf{x})$. Combing equations (2) and (3) leads to the final propagation equation

$$U_s(\omega, x = r, z = 0) = \mathbf{\Psi S}_u U_p(\omega, \mathbf{x}) T(\mathbf{x}). \tag{4}$$

Equation (4) can be written in a concise matrix form as

$$\mathbf{d} = \mathbf{Lm}, \tag{5}$$

where $\mathbf{L} = \mathbf{\Psi S}_u U_p(\omega, \mathbf{x})$ is the forward operator that produces the data $\mathbf{d} = U_s(\omega, x = r, z = 0)$ for a given model $\mathbf{m} = T(\mathbf{x})$. The aim of migration is to solve for the transmission coefficient $T(\mathbf{x})$ by taking the adjoint of the individual term in equation (4)

$$\hat{T}(\mathbf{x}) = U_p^*(\omega, \mathbf{x}) \mathbf{S'}_u \mathbf{\Psi'} U_s(\omega, x = r, z = 0), \tag{6}$$

and in the matrix form

$$\hat{\mathbf{m}} = \mathbf{L'd}, \tag{7}$$

where $\mathbf{L'}$ is the migration (adjoint) operator that maps the data to model space. Depending on the migration method, the operator $\mathbf{L'}$ can be designed using ray-theory, wave-equation propagator, or finite-difference modeling approaches.

2.2 Least-squares migration

LSM formulates the migration as a minimization problem (Nemeth et al., 1999). Typically, LSM utilizes iterative inversion to minimize the cost function of the following form

$$J = \|\mathbf{d} - \mathbf{Lm}\|_\mathbf{2}^\mathbf{2}, \tag{8}$$

which consists of the L-2 norm of the data misfit. This allows conveniently imposing smoothness constraints on the cost function

$$J = \|\mathbf{d} - \mathbf{Lm}\|_\mathbf{2}^\mathbf{2} + \mu \|\mathbf{Dm}\|_\mathbf{2}^\mathbf{2}, \tag{9}$$

where $\mathbf{D}$ can be a first-order differential operator that applies to smooth in the lateral direction. We modify the cost function defined in equation (9) by utilizing preconditioning, which is achieved by defining $\mathbf{u} = \mathbf{Dm}$ such that the model parameter can be written as $\mathbf{m} = \mathbf{Pu}$ with $\mathbf{P} = \mathbf{D^{-1}}$. The resulting preconditioned cost function is given by

$$J = \|\mathbf{d} - \mathbf{LPu}\|_\mathbf{2}^\mathbf{2} + \mu \|\mathbf{u}\|_\mathbf{2}^\mathbf{2}. \tag{10}$$

Optimization solvers such as the conjugate gradient (CG) method can readily minimize this cost function.

2.3 Forward and adjoint operators

The key to LSM is to design a pair of forward (de-migration) and adjoint (migration) operators that enable us to turn the migration process into a constrained least-squares minimization problem. In this study, we use the Split-step Fourier method to propagate the wavefield and migrate the RFs (Stoffa et al., 1990). This method properly accounts for laterally varying velocity structures through a two-step process in the frequency-wave number (f-k) and frequency-space (f-x) domains. We consider the acoustic wave equation

$$\nabla^2 p - u^2 \frac{\partial^2 p}{\partial t^2} = 0, \tag{11}$$

and its frequency domain form

$$\nabla^2 P + \omega^2 u^2 P = 0, \tag{12}$$

where $P(x, z, \omega)$ is the Fourier transform of the pressure field $p(x, z, t)$ (i.e., $P(x, z, \omega) = \int_{-\infty}^{\infty} p(x, z, t) e^{-i\omega t} dt$) and $u = u(x, z)$ is the slowness of a two-dimensional (2D) heterogeneous media. The slowness field $u(x, z)$ can be decomposed into two components, including a background term and a perturbation term

$$u(x, z) = u_0(z) + \Delta u(x, z), \tag{13}$$

where $u_0(z)$ represents the average slowness within each depth interval and $\Delta u(x, z)$ is the slowness perturbation that accounts for the lateral velocity variation. The Split-step Fourier method first extrapolates the wavefield in the f-k domain using the mean slowness within a depth interval Δz

$$P_1(k_x, z_n, \Delta z, \omega) = P(k_x, z_n, \omega) e^{ik_{z_0} \Delta z}, \tag{14}$$

where $P(k_x, z_n, \omega) = \int_{-\infty}^{\infty} P(x, z_n, \omega) e^{-ik_x x}$ is the up-going wavefield at depth z_n in the f-k domain, and k_x is the horizontal wavenumber and and k_{z_0} is the vertical wavenumber that correlates to average slowness by $k_{z_0} = \sqrt{\omega^2 u_0^2 - k_x^2}$. Equation 14 essentially applies a phase shift to wavefields at all frequencies and horizontal wavenumbers. Then we apply the inverse Fourier transform to map the wavefield from wavenumber to space to obtain the wavefield in the f-x domain

$$P_1(x, z_n, \Delta z, \omega) = (\frac{1}{2\pi})^2 \int_{-\infty}^{\infty} P_1(k_x, z_n, \Delta z, \omega) e^{ik_x x} dk_x. \tag{15}$$

The second step applies the time correction to each spatial location x to consider the lateral variation in slowness field $u(x, z)$

$$P(x, z_{n+1}, \omega) = e^{i\omega \Delta u(x,z) \Delta z} P_1(x, z_n, \Delta z, \omega). \tag{16}$$

Finally, we integrate over all frequencies of interest and apply inverse Fourier transform from the frequency domain back to time to obtain the migrated data in the time-space (t-x) domain at the next depth level z_{n+1}

The forward and adjoint operators are implemented similarly using the split-step method. In our implementation, the forward operator propagates both the P and S waves upward to the receiver (Figure 1a). The adjoint operator conducts backward (downward) propagation of the S wave from the receiver (Figure 1b). In RF migration, the up-going wavefields comprise the teleseismic P waves U_p incident below the recording array and the S waves U_s from the P-to-S conversions. The migration process backward propagates the converted S wave. The conversion point is located by applying the imaging condition with the cross-correlation form $T(\mathbf{x}) = U_s(\omega, \mathbf{x}) U_p^*(\omega, \mathbf{x})$ (see Figure 1b). The obtained migration image $T(\mathbf{x})$ is a scaled version of the true transmission coefficients.

A few modifications are required to implement LSM in the context of teleseismic RF imaging. First, point sources are placed at the bottom of the model to simulate the

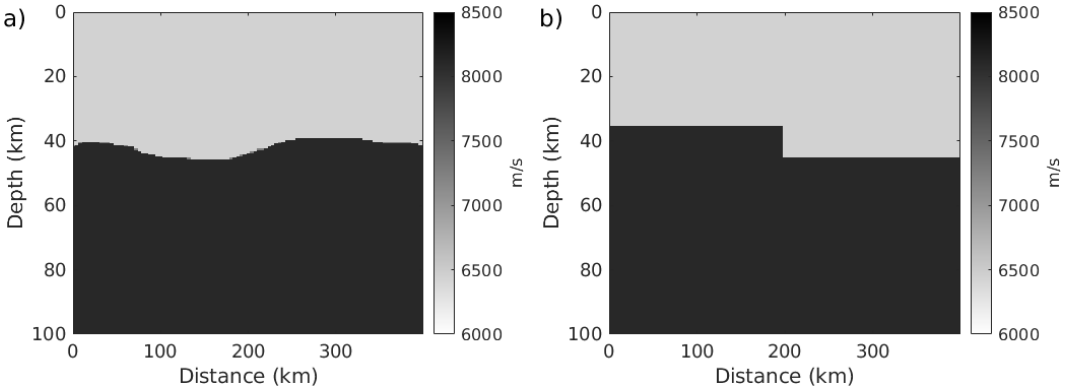

Figure 2. Synthetic models that contain (a) an undulated and (b) a step Moho. The colorbar indicates the P wave velocity.

plane-wave wavefield, with its incidence angle calculated with the ray parameter and the velocity at the bottom of the model. Point sources are excited consecutively with a time delay determined by the incidence angle, velocity, and separation distance. The source-time function is approximated by tapering the direct P wave around 0 times on the RFs. Second, the relative travel times of direct P waves between receivers need to be correctly restored. This considers the fact that the P waves are all aligned at 0 times after deconvolution. To recover the absolute travel time and obtain the receiver-side wavefield with the correct travel-time information, we apply time shifts to RFs according to travel times from the simulated P-wave wavefield (supplementary Figure S1). Third, because the acoustic wave equation is adopted, the P and S wave propagation must be performed separately with corresponding wave speeds. In the migration process, we utilize P-wave velocity to simulate the upgoing P-wave wavefield and corresponding S-wave velocity to simulate the downgoing S-wave wavefield.

3 Synthetic tests

To examine the proposed LSM approach, we conduct a 2D wavefield simulation with the SOFI2D code (Bohlen et al., 2016). This code implements a finite-difference scheme to solve the elastic wave equation. This method achieves a 2nd order accuracy in space and a 4th order accuracy in time. The free surface condition is applied to the top interface, and the absorbing boundary condition that implements perfectly matched layers (PMLs) (Komatitsch & Martin, 2007) is applied to the other three interfaces. We adopt a Ricker wavelet with a center frequency of 1 Hz. To simulate the teleseismic P-wave plane wave incidence, we place the point sources along a dipping plane and excite all point sources simultaneously. The vertical and horizontal components are used for RF calculation based on the iterative time-domain deconvolution method (Ligorría & Ammon, 1999).

We perform two synthetic tests using two-layer models with varying model geometry. The first model contains an undulated Moho geometry with a maximum depth variation of 10 km (Figure 2a) and the second model includes a Moho step with an offset of 10 km at the lateral distance of 200 km (Figure 2b). The migration velocity model is a smoothed version of the actual model. We simulate 10 teleseismic events with varying incidence angles from -20 to 20 deg at a 4-deg increment (the vertical incidence ray with an angle of 0 deg is excluded). We restore the correct P-wave travel times on RFs by cross-correlating their waveforms with the simulated P-wave wavefield. The time lag that leads to the maximum cross-correlation value is used as the amount of time shift applied to RFs.

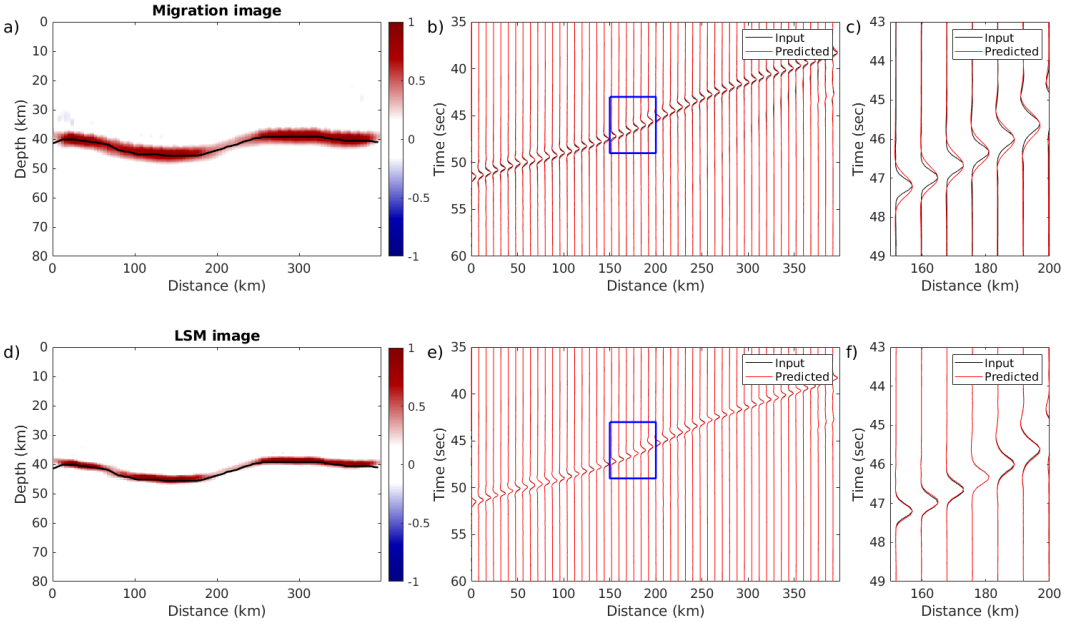

Figure 3. Migration imaging results of a single teleseismic event using an input model that contains an undulated Moho. (a) Migration image. The black line indicates the true Moho location. (b) Waveform fit predicted from the migration image. (c) Zoom-in plot shows details of the waveform fit. (d)-(f) The same as (a)-(c) but for least-squares migration imaging.

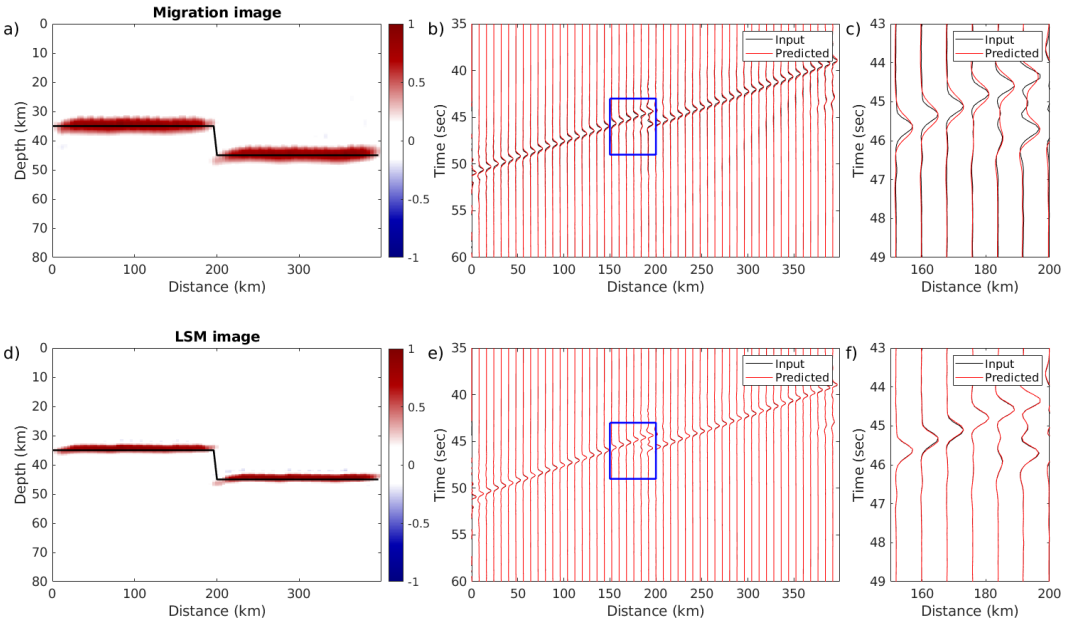

Figure 4. Migration imaging results of a single teleseismic event using an input model that contains a Moho step. See Figure 3 captions for details of each subplot.

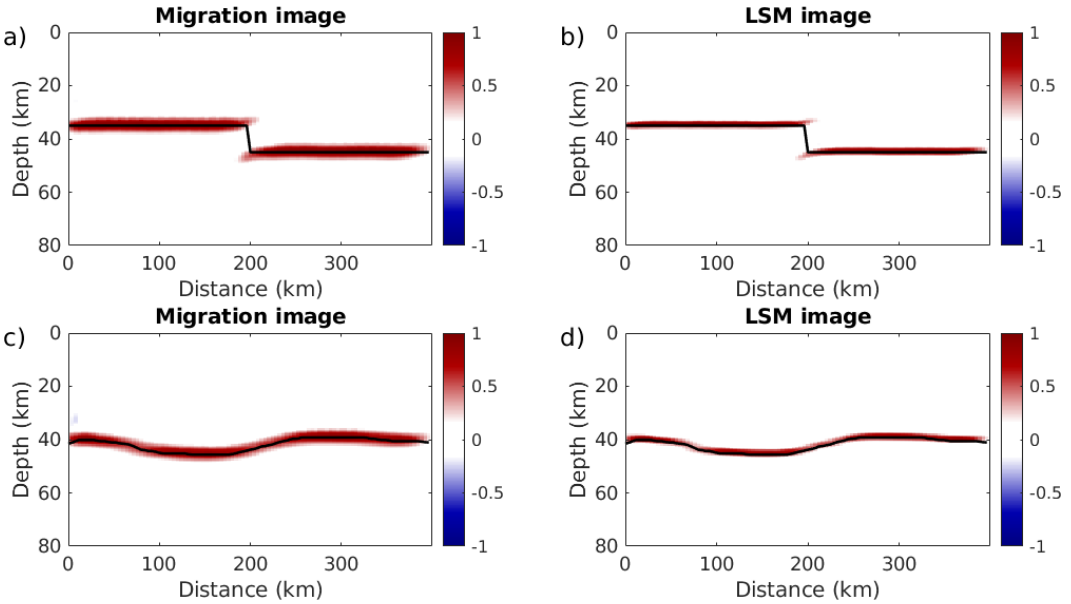

Figure 5. Comparison of stacked migration images of ten earthquakes from (a, c) migration and (b, d) least-squares migration.

We compare the imaging results from a single earthquake obtained using conventional migration and LSM (Figure 3). The traditional approach recovers the Moho well (Figure 3a). The predicted arrival times of Moho converted phases generally agree with observations, but the waveforms are broadened (Figures 3b-c). The resulting LSM image shows a sharper interface (Figure 3d). The corresponding waveform fit is significantly improved compared to the migration image (Figures 3e-f). A similar improvement is found in the test of the Moho-step model, where the interface is resolved at a higher vertical resolution in the LSM image with an improved waveform fit (Figure 4). The improvement in the migration result is more evident after stacking migration images from 10 earthquakes. The width of the Moho interface in the LSM image is about half that of the migration counterpart in both test cases (Figure 5). Note that the damping parameter in equation (10) controls the level of details in the model solution and a small value leads to improved data fit and sharper interfaces. However, a too small damping value can cause data overfitting and introduce imaging artifacts. In this test, we select a small damping value of 0.001 for the noise-free synthetic data to demonstrate the advantage of LSM. In real data application, one can construct an L-curve that demonstrates the trade-off between misfit and model norm and select the turning point as the optimal value.

4 Real data tests

4.1 Station and data

We perform a real data experiment using teleseismic earthquakes recorded by the Himalayan-Tibetan Continental Lithosphere during Mountain Building (Hi-CLIMB) seismic array. We select the central-northern portion of this semi-linear array that contains 70 stations with an average station spacing of about 8 km. The short station spacing is ideal for testing the proposed LSM method. We select events well aligned with the strike orientation of the seismic array to ensure that the wavefield can be approximated by the 2D simulation. Finally, 60 qualifying events are selected, with the majority located near the Sumatra and Java subduction zones (Figure 6).

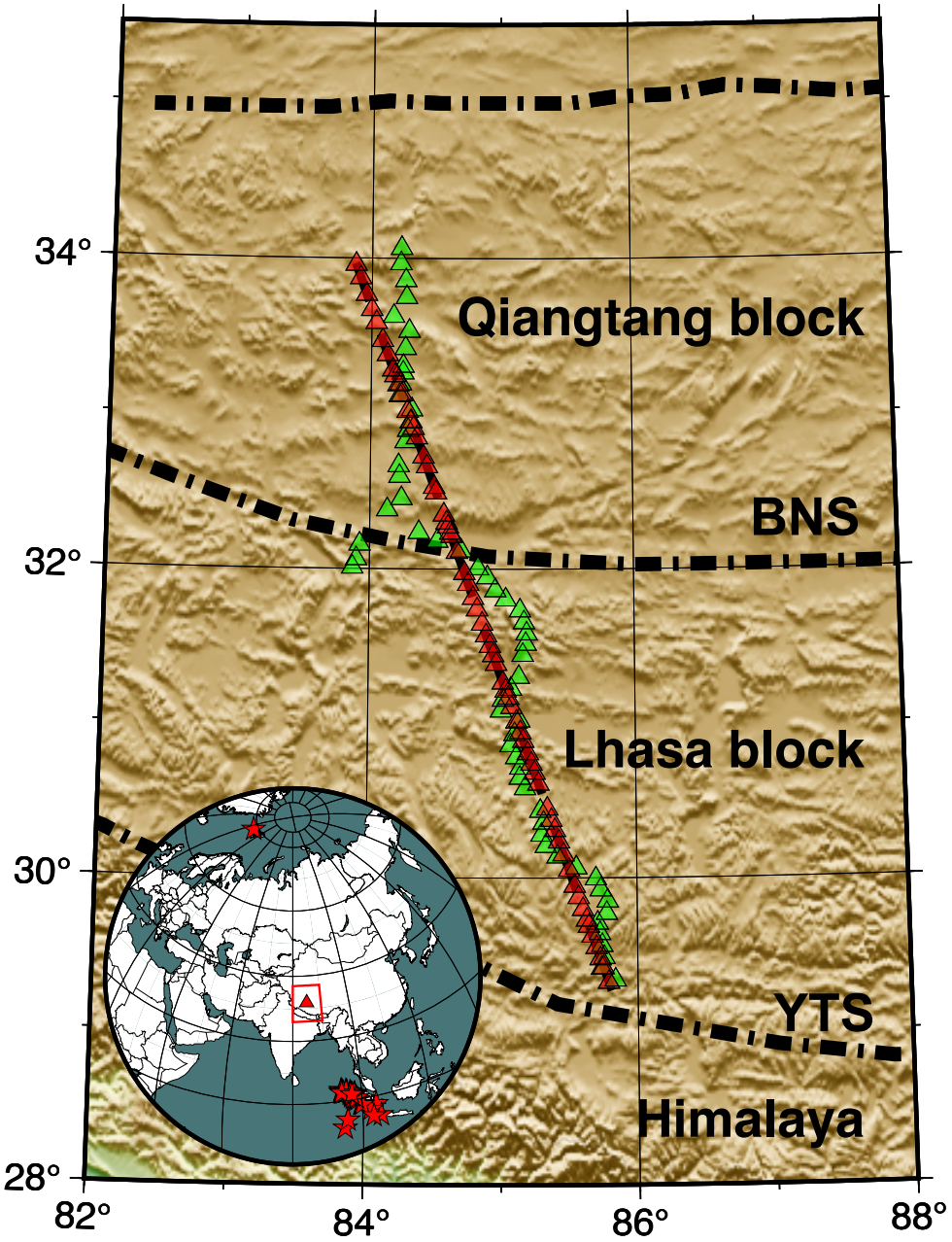

Figure 6. The Hi-CLIMB seismic array. The green triangles indicate the actual locations of seismic stations. The red triangles mark the projected locations onto the best fit great circle path. The inset map shows the distribution of earthquakes (stars). The red polygon highlights the study area with the seismic array indicated by the red triangle. Abbreviations: BNS-Bangong Nujiang Suture, YTS-Yarlung Tsangpo Suture.

4.2 Receiver function processing workflow

We summarize the processing workflow of the proposed migration imaging method in Figure 7. Several signal improvement steps are implemented before migration imaging considering the acquisition irregularity and noise contamination of the real data, which significantly degrade the robustness of the migration imaging. In the preprocessing step, we first conduct preliminary quality control of the data by removing traces with a signal-to-noise ratio (SNR) less than 0.5. The SNR is defined by the ratio of the data variance in the P-wave arrival window (-5 to 5 sec of the predicted P-wave arrival time) to the variance of the noise window starting 100 sec before the P-wave window. The P-wave segment of the three component seismograms, taken 30 sec and 120 sec before and after the theoretical P-wave arrival time, is filtered between 0.02 and 3 Hz with a Butterworth bandpass filter. Unlike the conventional RF processing workflow that directly invokes deconvolution to compute RFs, we implement a recently proposed preprocessing scheme based on the high-resolution Radon transform (Q. Zhang et al., 2022). The Radon transform is applied to radial- and vertical-component seismograms to improve the coherency of the useful signal while suppressing the random noise. This method is particularly well suited to regularizing wavefields and stabilizing the deconvolution process. The RFs are calculated with the regularized wavefields using the iterative time-domain deconvolution and a Gaussian parameter of 2.5. Because our implementation of wave propagation requires a regular grid, we group the irregularly distributed RFs into bins of the same size as the grid cell used in migration imaging to minimize data smoothing. The binning process leads to data gaps that cause discontinuous wavefield. We interpolate the missing traces with the Singular Spectrum Analysis (SSA) filter (Oropeza & Sacchi, 2011). This method assumes that a seismic wavefield is (locally) composed of plane waves that can be approximated by a low-rank matrix, while the presence of gaps and noises in the data can increase the rank. Therefore, data interpolation and noise removal can be accomplished by restoring the low-rank structure of the seismic data. This rank-reduction method has been applied to improve the quality of RFs in 2D (Dokht et al., 2017) and higher (4D and 5D) dimensions (Rubio et al., 2021). These individual processing steps are concatenated into an effective workflow that enables preconditioning of the data for the subsequent migration imaging (see Figure 7). We demonstrate the necessity and importance of the proposed workflow for exploiting the resolving power of LSM in section 5.1.

We show the results of critical processing steps in the proposed RF imaging workflow. First, the Radon-transform-based wavefield regularization improves the SNR of the vertical- and horizontal-component seismograms. The resulting denoised RF section shows clear Moho converted phases and secondary intra-crustal and lithospheric mantle conversions (Figure 8). For more details on the theory of Radon transform and parameter tuning in data processing, we refer readers to Q. Zhang et al. (2022). After binning the denoised RFs, about 60% percent of the traces are missing (Figure 9a). The reconstruction with SSA significantly enhances the RF quality and restores the continuous wavefield that is advantageous for migration imaging (Figure 9b).

4.3 Migration imaging

We compare the imaging results from the two migration methods. The velocity model is constructed according to Nowack et al. (2010) and contains two layers separated by the Moho with a gentle ramp (Supplementary Figure S2). The processed RFs (Figure 10a) are first migrated with the conventional approach. The migration image from a single event shows clear energy at about 60 km depth, which agrees with the Moho converted phases in this region (Figure 10b). The migration image also reveals significant interfaces in the crust and mantle. For example, positive phases are observed between 20-40 km and 100-130 km depth ranges. The predicted RFs from the migration model successfully reproduces the main arrivals but are characterized by broader waveforms (Fig-

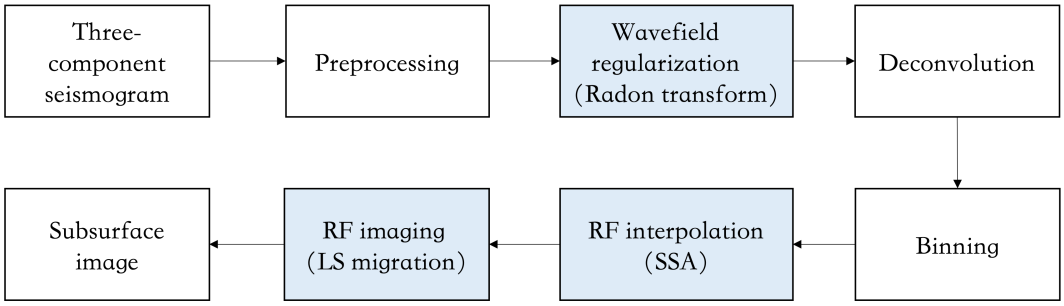

Figure 7. A flowchart showing the proposed receiver function processing and imaging workflow. The steps that are different from or not included in conventional receiver function imaging workflows are highlighted in blue.

ure 10c) compared to the observed RFs (Figure 10a). In comparison, the LSM result shows similar structures (Figure 11b), and the improvement in resolution is most evident from sharper interfaces and more finer-scale structures. The predicted RF records fit well with the observations and successfully recover detailed waveform features (Figure 11c).

We select 48 qualifying events and compare the stacked migration images from the two methods. The stacking process enhances structural coherency and leads to much-improved imaging of the subsurface (Figure 5) and, consequently, both migration images reveal enhanced structural variations compared to that from a single event (see Figures 10 and 11). The superior performance of migration approach is evident from the recovery of high-amplitude converted energy across the entire profile. These conversions depict two segments of clear double-layered structure with average depth varying from 60 km in the south to 70 km in the north. The southern segment initiates at the Indus-Yarlung suture (IYS) and extends northward for about 200 km. A similar structure has been reported in earlier studies using CCP (Nábělek et al., 2009) and reverse time migration methods (Shang et al., 2017). Farther north, earlier studies have revealed significant variability in Moho morphology, which has been identified as either a disrupted interface characterized by short-wavelength converted energy (Nowack et al., 2010; Nábělek et al., 2009) or a well-defined lower layer but barely visible converted energy from shallow depths (Shang et al., 2017). While the latter observation is also confirmed by our migration image, our study also reveals a clearly resolved upper interface. The implications of these new seismic observations on regional tectonics will be discussed in section 5.4. Overall, the LSM image reveals sharper interfaces and more structural details than the migration image. For instance, the top and bottom interfaces of the double-layered structures are better separated, and some weak phases, such as the top interface in the distance range of 350-450 km, also become more evident in the LSM image.

5 Discussion

5.1 Importance of data processing to migration imaging

We show that a proper data processing strategy is key to a robust application of migration imaging. Because the LSM imposes an L2-norm data misfit constraint to the cost function, which enforces a model solution that fits the data, the presence of noise inevitably introduces imaging artifacts to the migration result. Therefore, a well-designed processing workflow that ensures high-quality waveforms that contain reliable structural information is fundamental for the proposed RF imaging workflow. We use two data processing strategies to regularize wavefields, including the Radon transform and the SSA filter, which are implemented respectively before and after the deconvolution process.

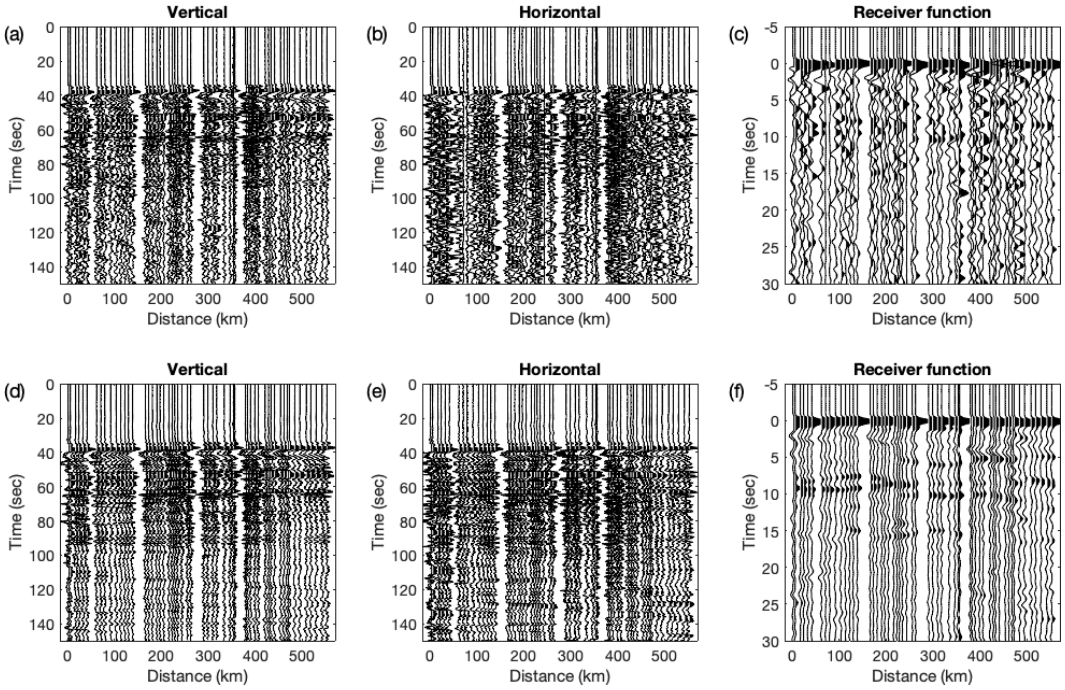

Figure 8. Wavefield regularization with the Radon transform. (a) Original vertical and (b) horizontal component seismograms. (c) Receiver functions are obtained from the raw data. (d) Vertical and (e) radial component seismograms were processed with the Radon transform. (f) Receiver functions obtained from denoised data.

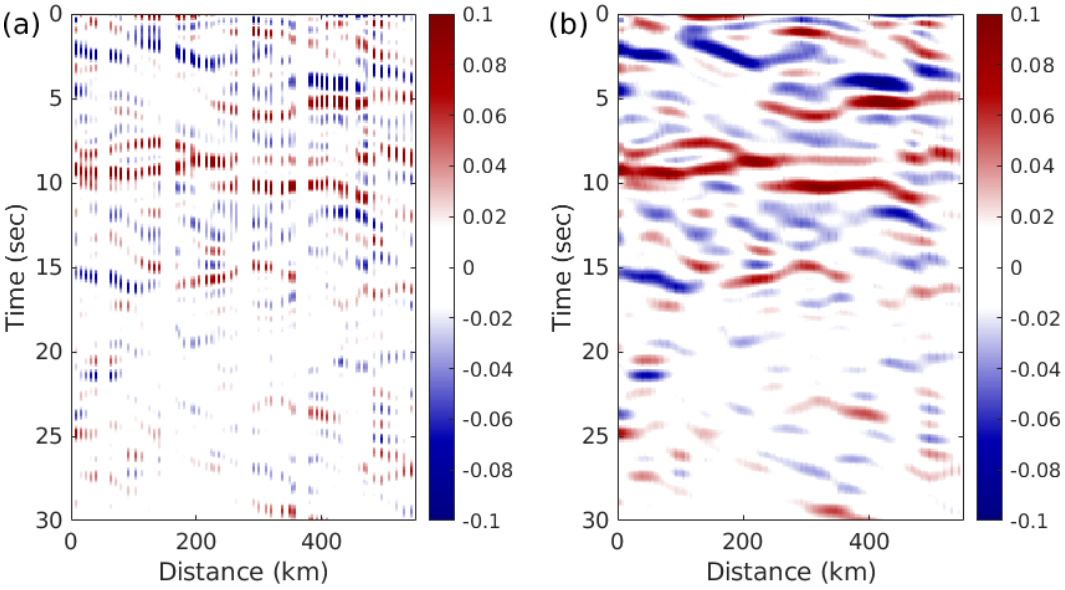

Figure 9. Receiver function (RF) interpolation using Singular Spectrum Analysis. (a) Binned and (b) reconstructed RFs.

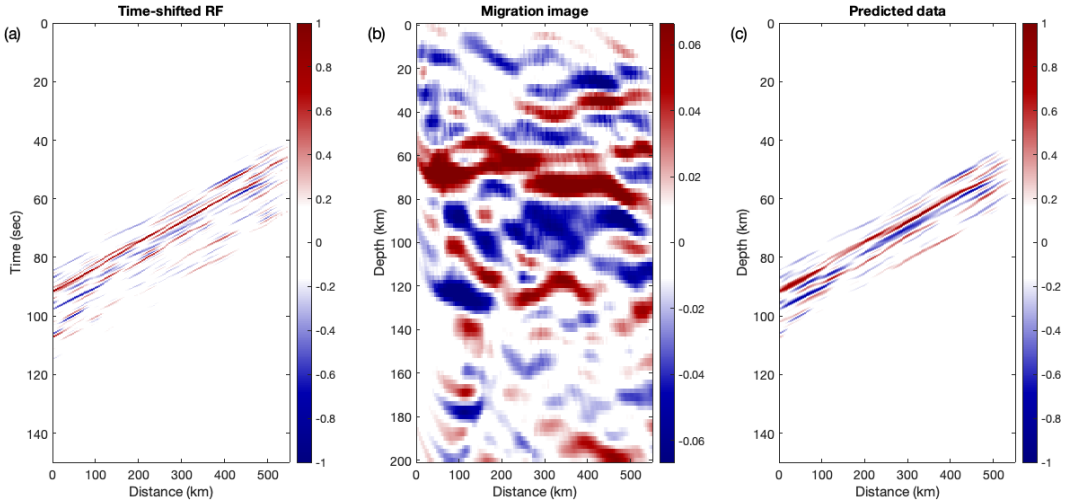

Figure 10. Migration results using processed receiver functions (RFs). (a) Observed RFs. (b) Migration image. (c) Predicted data.

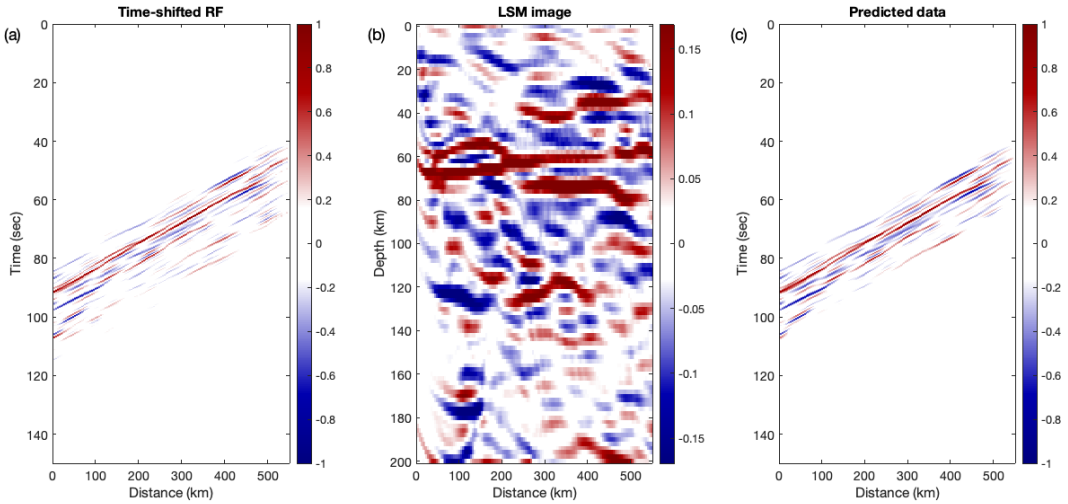

Figure 11. Least-squares migration results using processed receiver functions (RFs). (a) Observed RFs. (b) Migration image. (c) Predicted data.

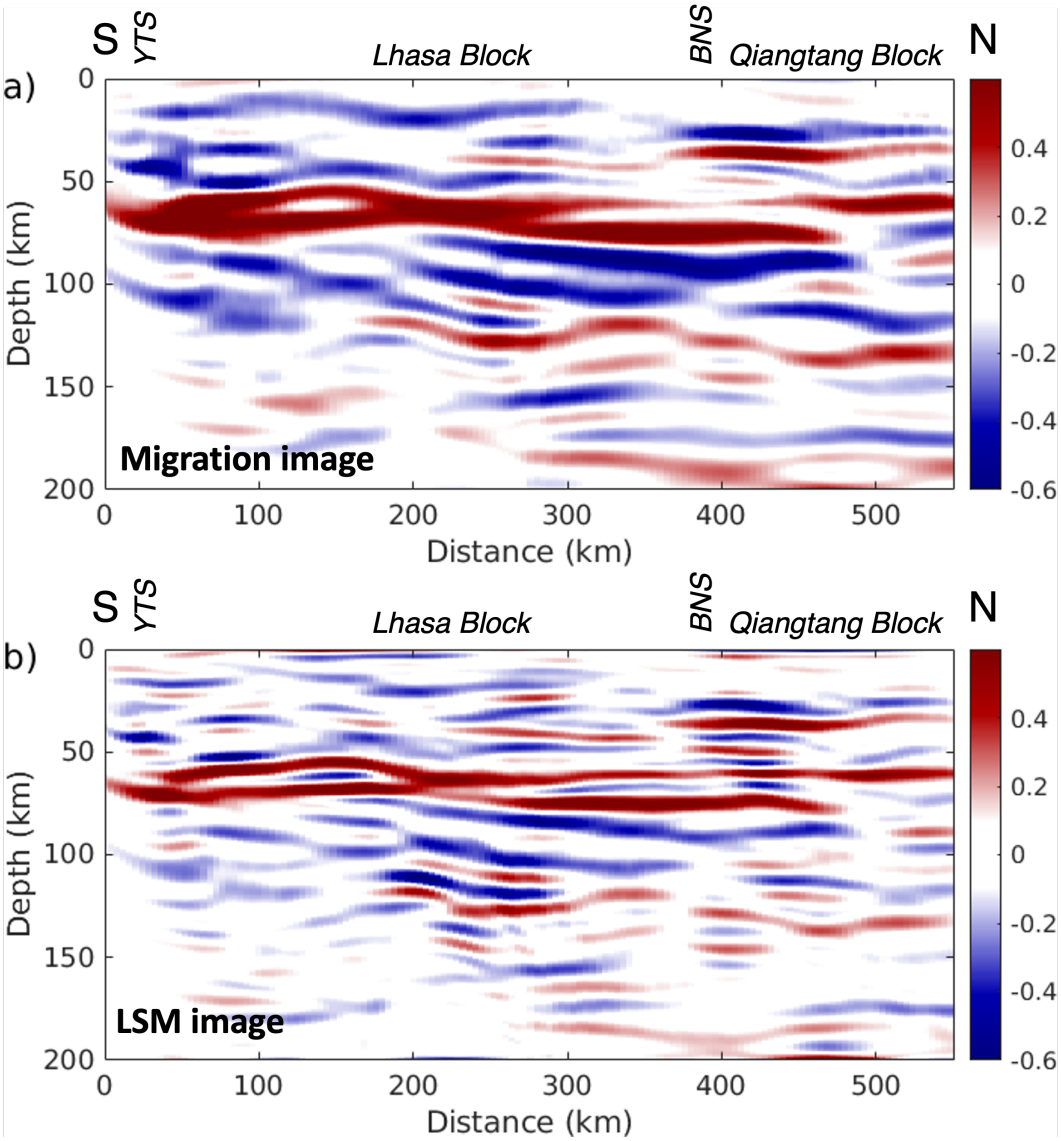

Figure 12. Receiver function migration results using 48 teleseismic events. (a) Migration image. (b) Least-squares migration image.

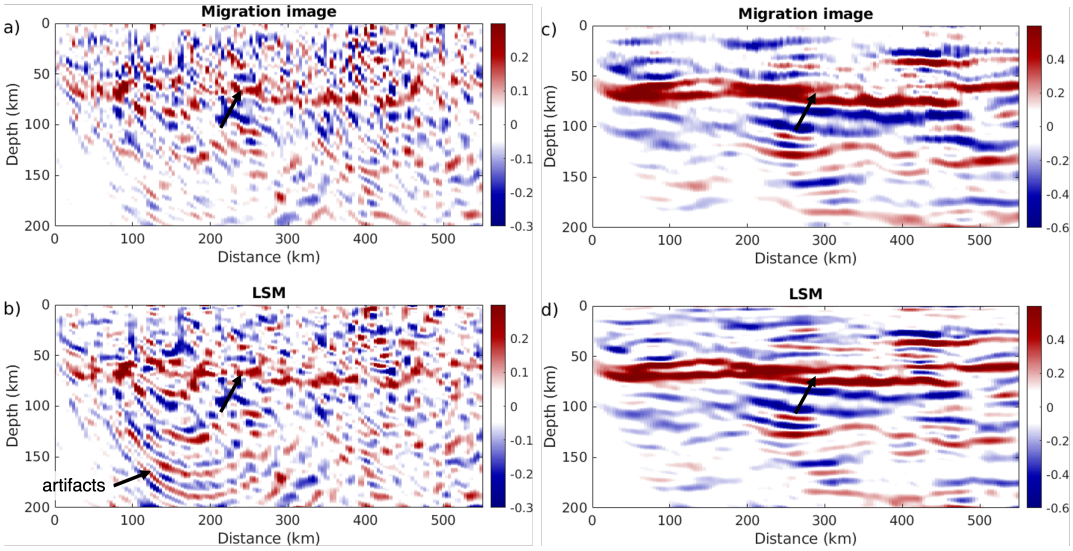

Figure 13. Comparison of migration results obtained from different data processing schemes. (a) Migration image without processing (i.e., using raw data). (b) Least-squares migration image without processing. (c) Migration image with the Radon transform only (i.e., without SSA). (d) Least-squares migration image with the Radon transform only. The arrows indicate imaging artefacts or poorly resolved interfaces.

We assess the effects of these data processing steps on the final migration images by directly migrating the unprocessed RFs. The raw migration image is characterized by small-scale structures throughout the profile with barely visible interfaces (Figure 13a). In addition, the intra-crustal and mantle interfaces are entirely overwhelmed by energy resembling random noise. In comparison, the LSM slightly improves the lateral continuity of the Moho interface but still exhibits abrupt variations (Figure 13b). The imaging quality significantly degrades in the deeper portion of the model, where sub-horizontal structures are absent and instead show curved interfaces with an ellipsoid shape. These steeply dipping structures are imaging artifacts caused by migrating traces contaminated by high-amplitude erratic noise.

In our workflow, the application of Radon transform regularizes the wavefield before the deconvolution and largely prevents the generation of erratic noise from the unstable devolution process. Migration images with the preprocessed RFs show 1) much-improved clarity and lateral continuity of crustal interfaces and 2) secondary mantle interfaces that are otherwise obscured by migration artifacts (Figures 13c and d). The SSA filter enables interpolating missing traces and reconstructing a complete wavefield. Migration imaging without SSA can capture the main structures, but the interfaces are more disrupted than those from reconstructed wavefields (see Figure 5a), showing moderate amplitude variations laterally (Figure 13c). The effects of wavefield irregularity are more severe in migration results of a single event (Supplementary Figure S3). Set side by side, the LSM image exhibits interfaces with more balanced energy than those from the conventional approach owing to the regularization term in the cost function (equation 9) that imposes a lateral smoothness constraint on the solution (Figure 13d). However, the secondary conversions from the crust and upper mantle are less well resolved than those migrated with the regularized wavefield (see Figure 5b). Several earlier studies of RF migration have also implemented various wavefield regularization strategies to improve migration imaging. Recent examples include using the curvelet transform (Shang et al., 2017)

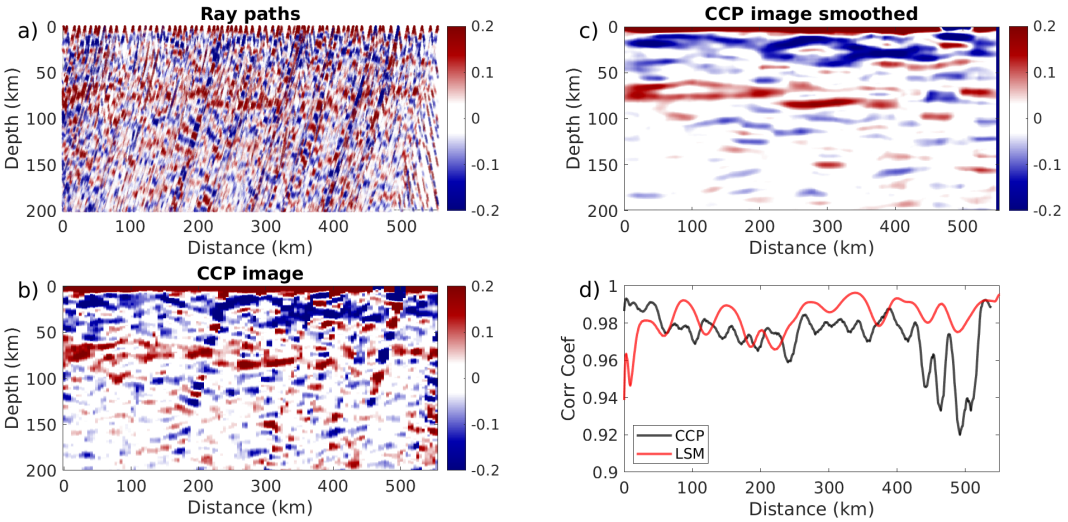

Figure 14. Common conversion point (CCP) imaging results. (a) Receiver functions (RFs) are back-projected along ray paths. (b) Raw CCP image obtained by binning and stacking RF amplitudes shown in (a). (c) Smoothed CCP image by applying a moving average filter to raw CCP image shown in (b). (d) Correlation coefficient between nearby traces in the CCP (black) and migration imaging profile (red).

and stretching-and-squeezing methods (Jiang et al., 2019) to interpolate missing seismic records. Our tests demonstrate that data preconditioning is a prerequisite to exploiting the resolving power of migration methods.

5.2 Effect of station spacing on migration imaging

One of the key concerns to applying the array-based seismic imaging technique is the station spacing. In traditional ray-theory approaches such as the common conversion point (CCP) stacking, the station spacing is approximately equivalent to the depth of the targeting structure to ensure that conversion points are overlapped. For wave-equation-based migration methods, the minimal station spacing is determined by the sampling theorem that requires at least two sampling points per wavelength to avoid spatial aliasing. According to L. Chen et al. (2005a), the maximum spatial sampling interval $\Delta x_{\max}$ is given by

$$\Delta x_{\max} \leq \frac{1}{2 f_{\max} p_{\max}}, \tag{17}$$

where $f_{\max}$ is the maximum frequency and $p_{\max}$ is the maximum horizontal slowness. We adopt a Gaussian parameter of 2.5 in the real data, corresponding to a maximum frequency of about 1.2 Hz. Considering a maximum horizontal slowness of 0.08 s/km for an epicentral distance of 30 deg, the required minimum station spacing is about 5 km. We adopt a bin size of 4 km in migration imaging, satisfying the sampling requirement. We examine the effect of large station spacing on migration by increasing the bin size to 8 km, roughly equivalent to the average station spacing. The resulting migration image is similar to the migration results using a 4-km wide bin, with slightly degraded imaging quality at shallower depths due to a lack of crisscrossing rays (Supplementary Figure S4). Our test suggests that the spatial sampling criterion can be slightly relaxed, but a station spacing of more than 10 km is recommended for the application of migration imaging.

5.3 Comparison with CCP imaging

The proposed migration imaging is compared with the CCP stacking method. It is worth noting that the imaging quality of CCP highly relies on processing parameters, particularly the bin size and overlapping distance between neighboring bins. To ensure a relatively fair comparison between the two approaches, we project the ray paths to the same 2D profile (Figure 14a) and attribute the unprocessed RFs to the same grid as that adopted in migration (i.e., 4 km laterally and 0.5 km vertically)(Figure 14b). The CCP profile shows small-scale structures likely resulting from random noise and incoherent phases. Primary crustal interfaces are better delineated than those from migration (see Figure 13a). In particular, the erratic noise is more focused without severely contaminating the nearby traces in the CCP image. This indicates that the CCP, which migrates the energy strictly along the ray paths, is more resistant to erratic noises of anomalous amplitude that otherwise introduce strong migration artifacts in LSM result (see Figure 13 b).

In practical applications, the clarity of the CCP image can be improved by adopting strategies of 1) utilizing large, overlapping bins when constructing the CCP gathers and 2) applying additional smoothing operators (e.g., moving average or Gaussian filter) to the original CCP image. We consider the second approach by applying a simple smoothing kernel with the size of 50×2 km (lateral×vertical) to the original CCP profile. The resulting image effectively suppresses small-scale structures and leads to more laterally coherent interfaces. However, the high-amplitude erratic noise is smeared and leaked into nearby areas (Figure 14c). Compared to the LSM results, the smoothed CCP profile is characterized by relatively broad waveforms of converted phases, weak amplitudes of major interfaces (e.g., Moho), and poor illumination and imaging artifacts in the deep (mantle) portion of the model. A quantitative comparison of the imaging results from the CCP and LSM is made by considering the lateral structural coherency. For each trace in the migration profile, we calculate an average correlation coefficient with its neighbouring traces within a lateral distance of 10 km. The LSM image leads to nearly consistently higher correlation coefficients than those from the CCP across the profile, particularly in the distance range of 400-500 km where the structural continuity is most severely affected by the erratic noise (Figure 14d). These comparisons suggest that our LSM workflow that applies proper wavefield regularization strategies is key to suppress the contaminating noise and render a subsurface image with improved structural coherency (see Figure 13c and d).

5.4 Advantage of improved imaging resolution

One fundamental goal of advancing seismic imaging techniques is to better resolve the subsurface structure for an improved understanding of regional tectonic processes. We briefly discuss how the improved subsurface image obtained from the LSM can contribute to this goal. The study region represents a collisional zone between the northward moving Indian Plate and the southward moving Eurasian Plate. The Hi-CLIMB array traverses several major tectonic boundaries, including the Bangong-Nujing Suture (BNS) and the Yarlung–Tsangpo Suture (YTS) (see Figure 6). Regional crustal structures have been investigated extensively by previous seismic studies. An earlier study conducted CCP imaging and revealed a double-layered system immediately to the north of the YTS near the southern end of the profile (Nábělek et al., 2009), which was interpreted as the upper and lower interfaces of the underplated lower crust of the Indian Plate. The lower crustal rocks were suggested to undergo high-grade metamorphism and were partially transformed into eclogite composition, resulting in a high impedance contrast at the upper interface. Farther north, the Moho becomes disrupted without a clear layered structure. In comparison, our LSM image reveals well-defined double-Moho structures along the entire profile, which can be subdivided into two distinctive segments (Figure 15). The northern segment is similar to that previously resolved by the CCP imag-

ing, whereas the southern segment extends continuously from the Lhasa Block across the BNS to the Qiangtang Block. This new observation and its formation mechanism can have important implications for regional tectonics.

We provide two possible interpretations for the observed two-layer structures. First, the southern segment may represent the eclogitized lower crust of the Tibetan Plate (Figure 15a), similar to the interpretation of its northern counterpart (Nábělek et al., 2009). Another mechanism attributes the southern segment to the imbricated crust of Tibetan and the Indian Plates formed by the underthrusting of the Indian lithosphere beneath Tibet (Figure 15b). The shallow and deep interfaces in this scenario are the Moho of the Tibetan and Indian Plates, respectively. This interpretation is further corroborated by the observations of dipping mantle interfaces that may represent the discontinuities within the underthrust Indian lithosphere. These two mechanisms can have different implications on the convergence process and the position of the collisional front of the Indian Plate. The former hypothesis suggests that the two plates converge at the joint of the two patches of the eclogitized lower crust (i.e., near 200 km distance), which is consistent with the location of the reported disruptive zone south of the BNS (Nábělek et al., 2009). The latter model could indicate that the leading edge of underthrusting Indian mantle extends well beyond the BNS into the Qiangtang Block (W.-P. Chen & Jiang, 2020). A more detailed investigation of these two hypotheses is beyond the scope of this work and will be summarized in a separate study.

5.5 Limitations and future improvements

Our synthetic and real data examples demonstrate several advantages of LSM in improving the resolution of RF imaging. However, the current implementation of LSM is limited by a few aspects: 1) it assumes that the energy in the RF mainly consists of converted waves; therefore, multiples (e.g., PpPms and PsPms+PpSms) cannot be migrated appropriately, and 2) it implements acoustic wave equation hence theoretically is only strictly applicable to P wave propagation, and 3) it simulates the wave propagation in 2D media, therefore, requires that a (semi-)linear array designed that is oriented approximately perpendicular to the strike of structures. The primary purpose of this study is to demonstrate the concept of LSM and examine its viability in teleseismic imaging, and future improvements can be readily implemented based on the current work. For instance, one can design the forward (de-migration) and migration operators according to elastic (Stanton & Sacchi, 2017) or two-way wave equations (Xu & Sacchi, 2018) such that the converted and multiple energy in RFs can be appropriately modeled. In addition, the current framework can be extended beyond 2D by considering the oblique incident wavefield (Bostock et al., 2001) and, alternatively, conducting 3D wavefield simulations using computationally efficient wave propagators (e.g., Duquet et al., 2000; Yang et al., 2018) or theoretically more rigorous reverse-time migration (Y. Zhang et al., 2015). These technique improvements allow us to incorporate teleseismic events from all azimuths to improve subsurface illumination. As importantly, we suggest that advances in imaging techniques must be accompanied by multi-dimensional data processing (Y. Chen et al., 2019; Rubio et al., 2021) to fully exploit the resolving power of the array-based seismic imaging method.

6 Conclusion

In this study, we propose a new teleseismic RF imaging method based on the concept of LSM. The key to our implementation of LSM is designing a pair of forward (de-migration) and adjoint (migration) operators using the split-step Fourier method, which enables us to turn migration imaging into a least-squares optimization problem. We utilize a cost function containing the L2 data misfit and model norm terms, with the former effectively constraining the waveform fit and the latter imposing the smoothness reg-

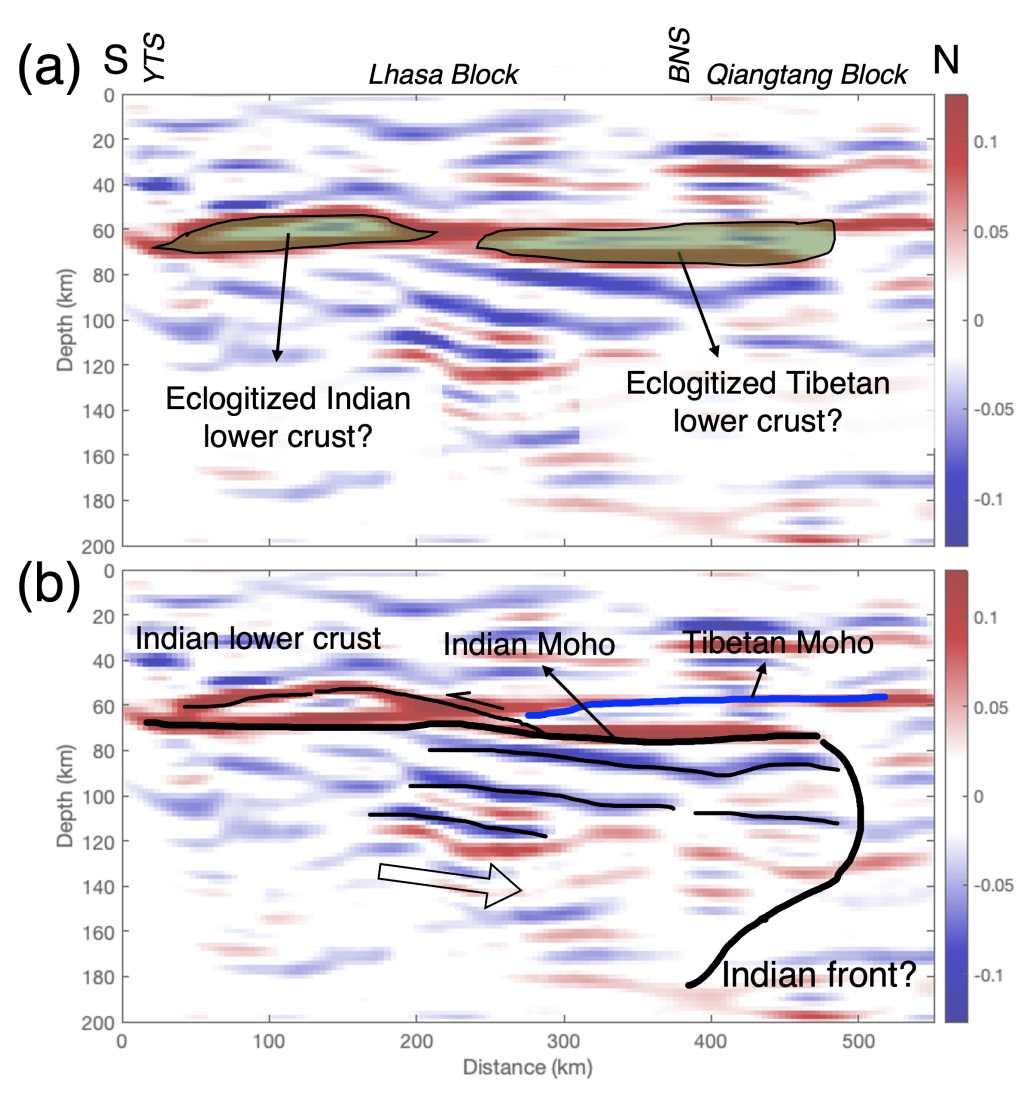

Figure 15. interpretation of key structures. Two models are proposed to explain the observed structures in the LSM image, including (a) eclogitized lower crust and (b) crust imbrication. The former model attributes the layered structure of the crust to the upper and lower boundaries of an eclogitized lower crustal layer. The southern and northern segments correspond to the Indian and Tibetan lower crust. In the second model, the Indian Plate underthrusts beneath the Tibetan Plate and potentially reaches the Qiangtang Block as inferred from the termination of dipping mantle interfaces, causing the imbrication of the (shallow) Tibetan Moho and the (deep) Indian Moho.

ularization to the model solution. We conduct two synthetic tests with varying Moho geometry to examine the robustness of the proposed LSM method. The test results show that the LSM is advantageous over the conventional migration methods in improving the vertical resolution of migration images. The migration of teleseismic recordings from the Hi-CLIMB array deployed on the Tibetan Plateau further demonstrates the capability of the LSM in enhancing the sharpness and lateral continuity of lithospheric discontinuities. The migration image resolves a well-defined double-Moho structure along the entire profile and better delineates secondary crustal and mantle interfaces. These new observations indicate that the collisional front of the underthrusting Indian Plate may reach at least as far north as the BNS, which sheds new light on the collision process between the Indian and the Tibetan Plates. To deal with the noise and irregularity in field data acquisition, we incorporate the Radon transform and the SSA filter into our migration imaging workflow. These processing steps allow regularizing wavefields and preconditioning RFs before migration. A comparison of migration images from the processed and raw RFs shows that data processing can significantly reduce migration artifacts caused by noisy data and improve the clarity of migration images. We strongly recommend adopting array data processing techniques in the RF migration workflow; otherwise, LSM may produce even worse migration images than those from the conventional CCP method. In conclusion, our study highlights the necessity and advantage of developing advanced array methods for better imaging of subsurface structures. The workflow proposed in this study also offers a basis for continuously improving the RF migration technique.

Acknowledgments

We thank Jinkun Cheng for providing the original version of the Split-step Fourier migration code. We thank Mauricio D. Sacchi for helpful discussions and proofreading an earlier version of the manuscript. The earthquake data from Hi-CLIMB array, network code XF, are available from IRIS Data Management Center.

References

Bohlen, T., De Nil, D., Köhn, D., & Jetschny, S. (2016). Sofi2d seismic modeling with finite differences: 2d—elastic and viscoelastic version. *Karlsruhe Institute of Technology, used under GNU General Public License, Free Software Foundation*.

Bostock, M., Rondenay, S., & Shragge, J. (2001). Multiparameter two-dimensional inversion of scattered teleseismic body waves 1. theory for oblique incidence. *Journal of Geophysical Research: Solid Earth*, *106*(B12), 30771–30782.

Chen, L., Wen, L., & Zheng, T. (2005a). A wave equation migration method for receiver function imaging: 1. theory. *Journal of Geophysical Research: Solid Earth*, *110*(B11).

Chen, L., Wen, L., & Zheng, T. (2005b). A wave equation migration method for receiver function imaging: 2. application to the japan subduction zone. *Journal of Geophysical Research: Solid Earth*, *110*(B11).

Chen, W.-P., & Jiang, Y. (2020). Undulating moho beneath a near-uniform surface of central tibet. *Earth and Planetary Science Letters*, *543*, 116343.

Chen, Y., Bai, M., & Chen, Y. (2019). Obtaining free usarray data by multi-dimensional seismic reconstruction. *Nature Communications*, *10*(1), 1–13.

Cheng, C., Bodin, T., & Allen, R. M. (2016). Three-dimensional pre-stack depth migration of receiver functions with the fast marching method: a kirchhoff approach. *Geophysical Journal International*, *205*(2), 819–829.

Cheng, C., Bodin, T., Tauzin, B., & Allen, R. M. (2017). Cascadia subduction slab heterogeneity revealed by three-dimensional receiver function kirchhoff migration. *Geophysical Research Letters*, *44*(2), 694–701.

Dokht, R. M., Gu, Y. J., & Sacchi, M. D. (2017). Singular spectrum analysis and its applications in mapping mantle seismic structure. *Geophysical Journal Interna-*

tional, *208*(3), 1430–1442.

Dueker, K. G., & Sheehan, A. F. (1998). Mantle discontinuity structure beneath the colorado rocky mountains and high plains. *Journal of Geophysical Research: Solid Earth*, *103*(B4), 7153–7169.

Duquet, B., Marfurt, K. J., & Dellinger, J. A. (2000). Kirchhoff modeling, inversion for reflectivity, and subsurface illumination. *Geophysics*, *65*(4), 1195–1209.

Gray, S. H., Etgen, J., Dellinger, J., & Whitmore, D. (2001). Seismic migration problems and solutions. *Geophysics*, *66*, 1622–1640.

Hansen, S., & Schmandt, B. (2017). P and s wave receiver function imaging of subduction with scattering kernels. *Geochemistry, Geophysics, Geosystems*, *18*(12), 4487–4502.

Jiang, X., Zhu, L., Hu, S., & Huang, R. (2019). Three-dimensional reverse-time migration of teleseismic receiver functions using the phase-shift-plus-interpolation method. *Geophysical Journal International*, *217*(2), 1047–1057.

Komatitsch, D., & Martin, R. (2007). An unsplit convolutional perfectly matched layer improved at grazing incidence for the seismic wave equation. *Geophysics*, *72*(5), SM155–SM167.

Kühl, H., & Sacchi, M. D. (2003). Least-squares wave-equation migration for avp/ava inversion. *Geophysics*, *68*(1), 262–273.

Langston, C. A. (1979). Structure under mount rainier, washington, inferred from teleseismic body waves. *Journal of Geophysical Research: Solid Earth*, *84*(B9), 4749–4762.

Li, J., Shen, Y., & Zhang, W. (2018). Three-dimensional passive-source reverse-time migration of converted waves: the method. *Journal of Geophysical Research: Solid Earth*, *123*(2), 1419–1434.

Ligorría, J. P., & Ammon, C. J. (1999). Iterative deconvolution and receiver-function estimation. *Bulletin of the seismological Society of America*, *89*(5), 1395–1400.

Millet, F., Bodin, T., & Rondenay, S. (2019). Multimode 3-d kirchhoff migration of receiver functions at continental scale. *Journal of Geophysical Research: Solid Earth*, *124*(8), 8953–8980.

Nábělek, J., Hetényi, G., Vergne, J., Sapkota, S., Kafle, B., Jiang, M., ... Team, t. H.-C. (2009). Underplating in the himalaya-tibet collision zone revealed by the hi-climb experiment. *Science*, *325*(5946), 1371–1374.

Nemeth, T., Wu, C., & Schuster, G. T. (1999). Least-squares migration of incomplete reflection data. *Geophysics*, *64*(1), 208–221.

Nowack, R. L., Chen, W.-P., & Tseng, T.-L. (2010). Application of gaussian-beam migration to multiscale imaging of the lithosphere beneath the hi-climb array in tibet. *Bulletin of the Seismological Society of America*, *100*(4), 1743–1754.

Oropeza, V., & Sacchi, M. (2011). Simultaneous seismic data denoising and reconstruction via multichannel singular spectrum analysis. *Geophysics*, *76*(3), V25–V32.

Phinney, R. A. (1964). Structure of the earth's crust from spectral behavior of long-period body waves. *Journal of Geophysical Research*, *69*(14), 2997–3017.

Poppeliers, C., & Pavlis, G. L. (2003a). Three-dimensional, prestack, plane wave migration of teleseismic p-to-s converted phases: 1. theory. *Journal of Geophysical Research: Solid Earth*, *108*(B2).

Poppeliers, C., & Pavlis, G. L. (2003b). Three-dimensional, prestack, plane wave migration of teleseismic p-to-s converted phases: 2. stacking multiple events. *Journal of Geophysical Research: Solid Earth*, *108*(B5).

Rondenay, S., Bostock, M., & Shragge, J. (2001). Multiparameter two-dimensional inversion of scattered teleseismic body waves 3. application to the cascadia 1993 data set. *Journal of Geophysical Research: Solid Earth*, *106*(B12), 30795–30807.

Rubio, G., Chen, Y., Sacchi, M. D., & Gu, Y. J. (2021). 3-d and 5-d reconstruc-

tion of p receiver functions via multichannel singular spectrum analysis. *Geophysical Journal International*, *225*(2), 1110–1128.

Ryberg, T., & Weber, M. (2000). Receiver function arrays: a reflection seismic approach. *Geophysical Journal International*, *141*(1), 1–11.

Sava, P., & Hill, S. J. (2009). Overview and classification of wavefield seismic imaging methods. *The Leading Edge*, *28*, 170–183.

Shang, X., de Hoop, M. V., & van der Hilst, R. D. (2017). Common conversion point stacking of receiver functions versus passive-source reverse time migration and wavefield regularization. *Geophysical Journal International*, *209*(2), 923–934.

Shragge, J., Artman, B., & Wilson, C. (2006). Teleseismic shot-profile migration. *Geophysics*, *71*(4), SI221–SI229.

Shragge, J., Bostock, M., & Rondenay, S. (2001). Multiparameter two-dimensional inversion of scattered teleseismic body waves 2. numerical examples. *Journal of Geophysical Research: Solid Earth*, *106*(B12), 30783–30793.

Stanton, A., & Sacchi, M. D. (2017). Elastic least-squares one-way wave-equation migration. *Geophysics*, *82*(4), S293–S305.

Stoffa, P., Fokkema, J. T., de Luna Freire, R., & Kessinger, W. (1990). Split-step fourier migration. *Geophysics*, *55*(4), 410–421.

Vinnik, L. (1977). Detection of waves converted from p to sv in the mantle. *Physics of the Earth and planetary interiors*, *15*(1), 39–45.

Wilson, D., & Aster, R. (2005). Seismic imaging of the crust and upper mantle using regularized joint receiver functions, frequency–wave number filtering, and multimode kirchhoff migration. *Journal of Geophysical Research: Solid Earth*, *110*(B5).

Xu, L., & Sacchi, M. D. (2018). Preconditioned acoustic least-squares two-way wave-equation migration with exact adjoint operatorleast-squares migration. *Geophysics*, *83*(1), S1–S13.

Yang, J., Zhu, H., McMechan, G., & Yue, Y. (2018). Time-domain least-squares migration using the gaussian beam summation method. *Geophysical Journal International*, *214*(1), 548–572.

Zhang, H., & Schmandt, B. (2019). Application of ps scattering kernels to imaging the mantle transition zone with receiver functions. *Journal of Geophysical Research: Solid Earth*, *124*(1), 709–728.

Zhang, Q., Chen, Y., Zhang, F., & Chen, Y. (2022). Improving receiver function imaging with high-resolution radon transform. *Geophysical Journal International*.

Zhang, Y., Duan, L., & Xie, Y. (2015). A stable and practical implementation of least-squares reverse time migration. *Geophysics*, *80*(1), V23–V31.

Zhu, L. (2000). Crustal structure across the san andreas fault, southern california from teleseismic converted waves. *Earth and Planetary Science Letters*, *179*(1), 183–190.